

A practical review on linear and nonlinear global approaches to stability analysis

D. Fabre^(a), V. Citro^(b), D. Ferreira Sabino^(a), P. Bonnefis^(a), & F. Giannetti^(b)

^(a) Institut de Mécanique des fluides de Toulouse (IMFT), University of Toulouse

^(b) Dipartimento di Ingegneria (DIIN), Università di Salerno.

This paper is aimed to review the linear and nonlinear approaches to study the stability of fluid flows. We provide a concise but self-contained exposition of the main concepts and specific numerical methods designed for global stability studies, including the classical linear stability analysis, the adjoint-based sensitivity and the most recent nonlinear developments. Regarding numerical implementation, a number of ideas making resolution particularly efficient are discussed, including mesh adaptation, simple shift-invert strategy instead of the classical Arnoldi algorithm, and a simplification of the recent nonlinear self-consistent approach proposed by Mantić-Lugo et al [1]. An open-source software implementing all the concepts discussed in the present paper is provided. The software is demonstrated for the reference case of the incompressible, two-dimensional flow around a circular cylinder, but is easily customisable to a variety of other flow configurations or flow equations.

1 Introduction

The concept of stability bears on the reaction of a system to a small perturbation of its state. If the generic disturbance grows in time, the system is unstable. The concept of stability can be simply formulated for a system of Ordinary Differential Equations (ODE). Such systems can be at equilibrium, where the state does not depend on time, or can present a periodic state, with all components returning to the same values, after every period.

The stability of fluid flows usually depends on the value of a given parameter. A bifurcation occurs when a critical value is reached and the original solution becomes linearly unstable, with the system tending towards a new steady or unsteady state. In the second part of the 19th century, specific analytical and numerical methods able to study these bifurcations have emerged and are continuously evolving up to the present days. A crucial point, that drove the development in this field, is the availability of larger and larger computing resources. Initially, the linear stability theory focused on fluid flows that are homogeneous in two spatial directions, e.g. plane Poiseuille flow [2]. This implies that the streamwise and the spanwise base-flow

gradients vanish and, as a consequence, it is possible to consider only one (streamwise) velocity component. Thus, the stability problem requires a *local* numerical resolution, i.e. a one-dimensional problem. On the other hand, when there are at least two spatial variables, the class of methods suited to solve such problems are generally called “global stability approaches”. A classical example of such behavior in fluid dynamics is the instability occurring in the wake of a circular cylinder. At low Reynolds number (precisely for $Re < 46.7$) the flow is steady and symmetric, but for larger values of Re a global instability arises in the flow field leading to the well-known von Kármán vortex alley. This flow configuration has served as a benchmark in the development of this class of methods. If one is only interested in predicting the stability or instability of a flow, it is enough to conduct a *linear stability analysis* which is the fundamental brick of global stability approaches. Beyond this simple question, in the past two decades, a number of extensions have been developed and popularized. *Adjoint methods* are an important extension [3], [4]; they can give insight into the sensitivity of the flow to intrinsic or extrinsic contributions. *Nonlinear stability approaches* [1], [5] have also been developed in order to extend the range of applicability of the approach towards large amplitude perturbations.

The objective of the present work is to contribute to the popularization of such methods in two ways:

First, we give a concise but self-contained exposition of the main concepts and specific numerical methods pertaining to global stability, including basic linear stability, adjoint-based sensitivity, as well as the most recent nonlinear developments.

Secondly we offer an open-source and user-friendly software called “StabFem”¹ to perform such calculations. The software combines program written in both FreeFem++ and Matlab languages. FreeFem++ is used to generate and adapt the meshes and to solve the various linear problems arising in the analysis. Matlab is used as a driver to monitor the computations, perform

¹The StabFem software may be obtained at the following url : <https://github.com/erbaDavid/StabFem>

the required loops over parameters, and plot the results.

In the present paper the concepts are introduced and the software is demonstrated for the reference case of the incompressible, two-dimensional flow around a cylinder, but the software is easily customizable to a variety of other situations (compressible, three-dimensional, etc.).

Although we don't claim to invent any radically new method, our exposition and implementation contains a number of originalities making the computation particularly efficient in terms of computational time and memory (all the figures of the paper can be produced in only a few minutes on a standard laptop)². The most notable originalities are the systematic use of mesh adaptation (§2 and 3), the use of simple shift-invert instead of Arnoldi (§3), and a reformulation and simplification of the nonlinear self-consistent approach of Mantic-Lugo et al (§4).

2 Linear stability analysis : equations and methods

2.1 Computing a base-flow with Newton iteration

Navier-Stokes equations and weak form We start from the general problem of a flow field $[\mathbf{u}, p]$ satisfying the incompressible Navier-Stokes equations on a domain Ω ,

$$\partial_t \mathbf{u} = \mathcal{N}(\mathbf{u}, p) \equiv -\mathbf{u} \cdot \nabla \mathbf{u} - \nabla p + \frac{2}{Re} \nabla \cdot \mathbf{D}(\mathbf{u}), \quad (1)$$

$$\nabla \cdot \mathbf{u} = 0, \quad (2)$$

with suitable boundary conditions on the frontier $\partial\Omega$ of the domain. Here $\mathbf{D}(\mathbf{u})$ is the rate-of-strain tensor defined as

$$\mathbf{D}(\mathbf{u}) = 1/2 (\nabla \mathbf{u} + \nabla^T \mathbf{u}),$$

In the framework of finite element methods, we need to write the equation in weak form. Prior to this we define a scalar product as follows, for either scalar or vectorial quantities $\langle \phi_1, \phi_2 \rangle$:

$$\langle \phi_1, \phi_2 \rangle = \int_{\Omega} \bar{\phi}_1 \cdot \phi_2 \, d\Omega,$$

The weak form of the Navier-Stokes equations is readily defined by introducing test functions $[\mathbf{v}, q]$ associated with the momentum and continuity equations, and integrating over the domain³

$$\forall [\mathbf{v}, q], \quad \partial_t \langle \mathbf{v}, \mathbf{u} \rangle = \langle \mathbf{v}, \mathcal{N}(\mathbf{u}, p) \rangle + \langle q, \nabla \cdot \mathbf{u} \rangle. \quad (3)$$

²All the figures contained in the present paper can be processed by launching a single Matlab script `SCRIPT_CYLINDER_ALLFIGURES.m`. On a MacbookPro (2018, 2.5Ghz, 16Go Ram), the execution time is 19.76 seconds for the results of the linear analysis (section 3) and 15. seconds for the results of the nonlinear analysis (section 4).

³In the simple presentation given here we have omitted the issue of boundary conditions. Details on way boundary conditions can be incorporated in the weak formulation through integration by parts can be found in appendix A.

Newton iteration We look for a steady base-flow $[\mathbf{u}_b, p_b]$ satisfying the steady Navier-Stokes equations, i.e. $\mathcal{N}(\mathbf{u}_b, p_b) = 0$. Suppose that we have a “guess” for the base flow $[\mathbf{u}_b^g, p_b^g]$ which almost satisfies the equations. We look for a better approximation under the form

$$[\mathbf{u}_b, p_b] = [\mathbf{u}_b^g, p_b^g] + [\delta \mathbf{u}_b, \delta p_b]. \quad (4)$$

Injecting (4) into the weak form (3) of the Navier-Stokes equations and developing up to linear terms in terms of the perturbation lead to $\mathcal{N}(\mathbf{u}_b^g, p_b^g) + \mathcal{L}\mathcal{N}_{\mathbf{u}_b^g}(\delta \mathbf{u}_b, \delta p_b)$, which can also be written in weak form as:

$$\begin{aligned} & \langle \mathbf{v}, \mathcal{N}(\mathbf{u}_b^g, p_b^g) \rangle + \langle q, \nabla \cdot \mathbf{u}_b^g \rangle \\ & + \langle \mathbf{v}, \mathcal{L}\mathcal{N}_{\mathbf{u}_b^g}(\delta \mathbf{u}_b, \delta p_b) \rangle + \langle q, \nabla \cdot \delta \mathbf{u}_b \rangle = 0, \end{aligned} \quad (5)$$

where $\mathcal{L}\mathcal{N}$ is the linearised Navier-Stokes operator, defined by its action on a flow field $[\mathbf{u}, p]$ as follows

$$\mathcal{L}\mathcal{N}_{\mathbf{u}}(\mathbf{u}, p) = -C(\mathbf{U}, \mathbf{u}) - \nabla p + \frac{2}{Re} \nabla \cdot \mathbf{D}(\mathbf{u}), \quad (6)$$

and C is the convection operator defined by

$$C(\mathbf{U}, \mathbf{u}) = (\mathbf{U} \cdot \nabla) \mathbf{u} + (\mathbf{u} \cdot \nabla) \mathbf{U}. \quad (7)$$

This problem can now be discretized by projecting upon a basis of Taylor-Hood $(u, v, p) \rightarrow (P2, P2, P1)$ finite elements. Noting δX the discretization of $[\delta \mathbf{u}_b, \delta p_b]$ this eventually leads to a matricial problem of the form $A \cdot \delta X = Y$. The procedure of Newton iteration is to solve iteratively this set of equations up to convergence. In our implementation, the algorithm is written in the Freefem++ solver *Newton_2D.edp* which is wrapped by the Matlab driver *Freefem_BaseFlow.m*.

2.2 Linear stability

Direct eigenvalue problem We study the onset of the instability within the linear theory by using a normal-mode analysis:

$$\mathbf{u}(\mathbf{x}, t) = \mathbf{u}_b(\mathbf{x}) + \varepsilon \hat{\mathbf{u}}(\mathbf{x}) e^{\lambda t}, \quad p(\mathbf{x}, t) = p_b(\mathbf{x}) + \varepsilon \hat{p}(\mathbf{x}) e^{\lambda t}, \quad (8)$$

where $\lambda = \sigma + i\omega$ is the eigenvalue, σ the amplification rate, ω the oscillation rate, $\hat{\mathbf{u}}, \hat{p}$ the eigenmodes, and ε a small parameter. The eigenmodes and the eigenvalues are the solution of the following eigenproblem:

$$\lambda \hat{\mathbf{u}} = \mathcal{L}\mathcal{N}_{\mathbf{u}_b}(\hat{\mathbf{u}}, \hat{p}), \quad (9)$$

or, in weak form:

$$\lambda \langle \mathbf{v}, \hat{\mathbf{u}} \rangle = \langle \mathbf{v}, \mathcal{L}\mathcal{N}_{\mathbf{u}_b}(\hat{\mathbf{u}}, \hat{p}) \rangle + \langle q, \nabla \cdot \hat{\mathbf{u}} \rangle. \quad (10)$$

After discretization, we end up with an eigenvalue problem with the matricial form

$$\lambda B \hat{X} = A \hat{X}, \quad (11)$$

where A is the matrix resulting from the discretization of $\mathcal{LN}_{\mathbf{u}_b}$, i.e. the same matrix appearing in the Newton computation of the base flow, and B is a “weight” matrix associated to the scalar product $\langle v, u \rangle = \int \bar{v} \cdot \mathbf{u} \, d\Omega$.

Adjoint eigenvalue problem and structural sensitivity

Developed in the two past decades, the concept adjoint modes has now become an unavoidable complement to the linear global stability approach. We here give a short summary of the definition and usefulness of this concept, we refer to Luchini & Bottaro [6] for further details. First of all, the *adjoint linearised Navier-Stokes operator* $\mathcal{LN}_{\mathbf{u}}^\dagger$ is defined thanks to the following property:

$$\begin{aligned} \forall (\mathbf{u}, p; \mathbf{v}, q), \quad & \left\langle \mathcal{LN}_{\mathbf{u}}^\dagger(\mathbf{v}, q), \mathbf{u} \right\rangle + \langle \nabla \cdot \mathbf{v}, p \rangle \\ & = \left\langle \mathbf{v}, \mathcal{LN}_{\mathbf{u}}(\mathbf{u}, p) \right\rangle + \langle q, \nabla \cdot \mathbf{u} \rangle. \end{aligned} \quad (12)$$

We can then define the adjoint eigenvalues and eigenmodes as the solutions of the eigenvalue problem

$$\forall (\mathbf{u}, p), \quad \lambda^\dagger \langle \hat{\mathbf{v}}, \mathbf{u} \rangle = \left\langle \mathcal{LN}_{\mathbf{u}}^\dagger(\hat{\mathbf{v}}, \hat{q}), \mathbf{u} \right\rangle + \langle \nabla \cdot \hat{\mathbf{v}}, p \rangle. \quad (13)$$

It can be shown [7] that the adjoint eigenvalues λ_k^\dagger are the complex conjugates of the direct eigenvalues λ_k .

Although the concept of adjoint operator may sound complicate, the resolution of the adjoint problem using finite elements methods is actually extremely easy. In effect, the scalar product used in the definition of the weak formulation and that appearing in the definition of adjoint being the same, the weak formulations of both problems are thus identical when exchanging the test functions and the unknown functions. Thus the matricial form of the discretized version of (13) is deduced from the one of the direct problem by a simple (Hermitian) transpose of the matrix:

$$\bar{\lambda}^\dagger B \hat{X}^\dagger = A^T \hat{X}^\dagger. \quad (14)$$

Adjoint eigenmodes are a powerful tool for investigating problems such as receptivity, transient growth, control and sensitivity (see the reviews of [8], [9], [6]). The simplest physical interpretation of an adjoint eigenmode is as follows : it corresponds to the initial condition which has maximum projection along the direction of the corresponding eigenmode. Thus, the adjoint of the most amplified mode corresponds to the optimal perturbation which will maximize the growth of energy in the limit of large time. In effect, one can prove that for $t \rightarrow \infty$ the

asymptotic behaviour of a solution with initial condition \mathbf{u}_i is given as :

$$\mathbf{u}(t) \approx \frac{\langle \hat{\mathbf{u}}^\dagger, \mathbf{u}_i \rangle}{\langle \hat{\mathbf{u}}^\dagger, \hat{\mathbf{u}} \rangle} e^{\lambda t} \hat{\mathbf{u}}.$$

The choice $\mathbf{u}_i = \hat{\mathbf{u}}^\dagger$ is the initial condition of norm unity which maximizes the first factor in this expression.

The adjoint eigenmode also allows us to introduce the so-called *structural sensitivity tensor* that is defined as

$$\mathbf{S}(\mathbf{x}) = \frac{\|\hat{\mathbf{u}}^\dagger\| \|\hat{\mathbf{u}}\|}{\langle \hat{\mathbf{u}}^\dagger, \hat{\mathbf{u}} \rangle}, \quad (15)$$

which has become popular in the recent years. This quantity is a direct and practical measure of the effect of perturbations of the linear operator on the eigenvalue. The region of the flow where $\mathbf{S}(\mathbf{x})$ reaches its maximum values is, thus, the region where the instability mechanism originates, and is often referred to as the *wavemaker region*.

Iterative methods for eigenvalue computations When it comes to the numerical resolution of generalized eigenvalue problems such as $AX = \lambda BX$ (or its adjoint version (14)), several methods are possible. Direct methods to compute the whole spectrum are both costly prohibitive and useless. A popular alternative is the use of iterative methods which allow us to compute a limited set of eigenvalues located in the vicinity of a “shift” value λ_{shift} . The simplest version of this method is the simple shift-invert iteration, which consists of solving iteratively the system

$$X^n = (A - \lambda_{shift} B)^{-1} B X^{n-1}.$$

It is easy to show that this iterative procedure quickly asymptotes to $X^{n+1} \approx (\lambda^{*-1})^n \hat{X}$ where \hat{X} is the eigenmode with largest λ^{*-1} (i.e. the one with eigenvalue λ closest to the shift).

When a good estimation of the eigenvalue is available, this method converges very rapidly and is very efficient, but it can only provide a single eigenvalue. If we want to compute a larger number of eigenvalues, we can revert to a generalized version of iterative methods, called Arnoldi methods [10]. The shift-invert version of the Arnoldi method is in fact the most commonly used method of the current time and is at the basis of both the popular matlab function `eigs` and the eigenvalue solver of FreeFem (i.e. ARPACK++). Our implementation in StabFem allows to chose between single eigenvalue computation (power method) and multiple eigenvalue computation (Arnoldi). The selection is made according to the parameter “nev” transmitted to the driver.

2.3 Mesh adaptation procedure

As for any numerical method, a crucial point in the numerical efficiency is the design of the mesh. The finite

```

1  bf = SF_Init('Mesh_Cylinder_Large.edp');
2  bf = SF_BaseFlow(bf, 'Re', 1);
3  bf = SF_BaseFlow(bf, 'Re', 10);
4  bf = SF_BaseFlow(bf, 'Re', 60);
5  bf = SF_Adapt(bf, 'Hmax', 10, 'InterpError', 0.01);
6  [ev, em] = SF_Stability(bf, 'shift', 0.04+0.74i, 'type', 'S');
7  bf = SF_Adapt(bf, em, 'Hmax', 10, 'InterpError', 0.01);
8  plotFF(bf, 'mesh'); % Figure 2a
9  plotFF(bf, 'ux', 'Contour', 'on', 'Levels', [0,0]); % Figure 2b
10
11 Re_Range = [2 : 2: 50]; Drag_tab = []; Lx_tab = [];
12     for Re = Re_Range
13         bf = SF_BaseFlow(bf, 'Re', Re);
14         Drag_tab = [Drag_tab, bf.Drag];
15         Lx_tab = [Lx_tab, bf.Lx];
16     end
17 plot(Re_Range, Drag_tab, 'b+'); %Figure 3a
18 plot(Re_Range, Lx_tab, 'b+'); % Figure 3b
19
20 Re_Range = [40 : 2: 100]; lambda_branch = [];
21 bf = SF_BaseFlow(bf, 'Re', 40);
22 [ev, em] = SF_Stability(bf, 'shift', .03+.72i, 'nev', 1, 'type', 'D');
23     for Re = Re_Range
24         bf = SF_BaseFlow(bf, 'Re', Re);
25         [ev, em] = SF_Stability(bf, 'nev', 1, 'shift', 'cont');
26         lambda_branch = [lambda_branch ev];
27     end
28 plot(Re_Range, real(lambda_branch), 'b+'); %Figure 4a
29 plot(Re_Range, imag(lambda_branch)/(2*pi), 'b+'); % Figure 4b

```

Fig. 1. Illustration of the usage of the StabFem software to produce an adapted mesh and study the base flow and the linear stability properties of the wake flow around a cylinder (extract from script *SCRIPT_CYLINDER_ALLFIGURES.m*)

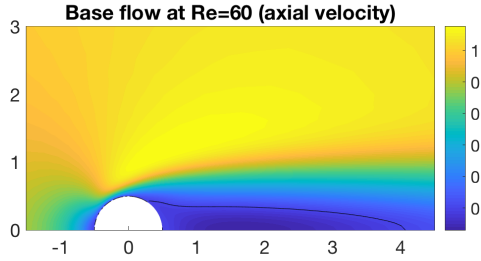


Fig. 2. Base flow (axial velocity component) for the flow over a cylinder at $Re = 60$.

element method allows to use unstructured mesh and hence to locally adapt the refinement. The most common procedure is to decompose the domain into several parts with different grid densities; for instance for the wake of a cylinder, we will design a near-wall region with very small size, a “wake” region with intermediate mesh size, and an outer region with large mesh size. The inconvenient is that the design relies on an a priori expectation of the regions where gradients will be large.

In our implementation, we used an automatic mesh adaptation method. The implementation relies on the

AdaptMesh procedure of the FreeFem++ software. This procedure is detailed in detail in ref. [11]. In short, the classical Delaunay-Voronoi algorithm produces a mesh with gridpoint distribution specified by a *Metric* matrix \mathcal{M} . The AdaptMesh algorithm consists of using as a metric the *Hessian* (second-order spatial derivatives) of an objective function u_h defined over the domain, i.e. $\mathcal{M} = \nabla \nabla u_h$. The precision can be controlled by specifying an objective value for the interpolation error of the function on the new mesh.

To build an optimal mesh for the base-flow calculation, the idea is to use as the objective function u_h the solution \mathbf{u}_b itself, as computed on a previous mesh. The base flow is then recomputed on the adapted mesh, providing a better approximation of the solution. The procedure can be repeated a few steps to ensure a right convergence.

The mesh generated in the previous way may not be optimal for the stability calculations as the structure of the eigenmode may be more complex than that of the base flow. To remedy with this, the idea is to subsequently adapt the mesh to both the mesh flow and the results of the stability calculation. This is easily done with FreeFem, as the AdaptMesh procedure can be used with several objective functions. We have experimented two different ideas. The first is to adapt the mesh to the base flow and the structure of the leading eigenmode. A second and smarter idea is to adapt the mesh to the base flow and the structural sensitivity. This

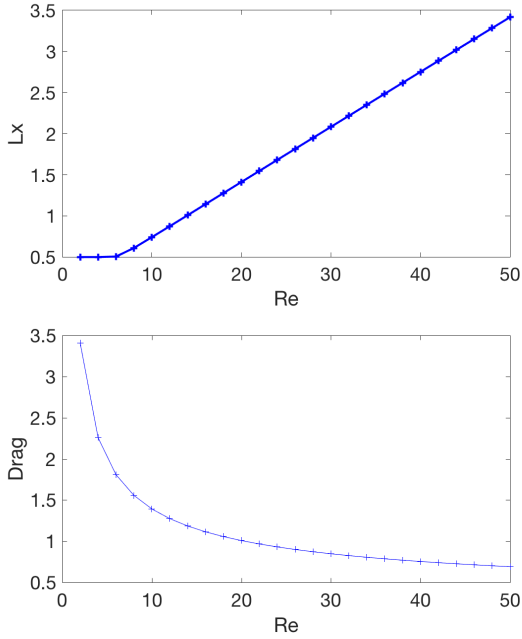


Fig. 3. Recirculation length L_x (a) and nondimensional drag F_x (b) of the base flow over a cylinder as function of Re .

idea is supported by Giannetti & Luchini [3] who showed that the accuracy of the stability results for the flow past a circular cylinder is strictly related to the mesh characteristics in the wavemaker region, i.e. the region where the structural sensitivity reaches its maximum values. Results show that the two procedures yield the same values for the eigenvalues with less than 1% error, but that the second method gives a mesh with about 3 times less grid points, leading to much faster computations (see appendix D). So, if one is interested only in the eigenvalues, for instance to plot growth rates as function of Reynolds or to identify the critical Reynolds number, mesh adaptation to the sensitivity gives the best option. On the other hand, if one is interested in the detailed structure of the eigenmode, which may extend far away from the wavemaker region, it is advised to use mesh adaptation on the eigenmode.

In our implementation, the whole process is performed using the Matlab driver *FreeFemAdaptMesh.m*; the kind of adaptation (to base flow only, to eigenmode, or to sensitivity) is decided by the choice of parameters transmitted to this function.

3 Illustration for the wake of a cylinder

Problem description Here, we consider the two-dimensional flow of an incompressible fluid of density ρ past a circular cylinder. All flow quantities are normalized using the uniform incoming velocity U_∞ and the cylinder diameter D , which are the characteristic velocity and length scales used for the definition of Reynolds number $Re = U_\infty D / \nu$. The origin of the cartesian frame of reference is considered located on the cylinder axis, the x-axis is chosen to be parallel to the incoming free-stream

velocity while the y-axis with the cross-stream velocity. The dimensions of the computational domain are the following: $-40 \leq x/D \leq 80$ and $-40 \leq y/D \leq 40$. We impose a no-slip condition ($u = 0, v = 0$) on the cylinder surface (Γ_{cyl}), a uniform velocity ($u = 1, v = 0$) at the inflow $x/D = -40$ and a no-stress condition at the outlet $x/D = 80$ and on the lateral boundaries of the computational domain $y/D = \pm 40$.

The hydrodynamic loads can be obtained by integrating the stress tensor over the cylinder surface. In particular, the hydrodynamic lift and drag forces read⁴

$$F_x = \mathcal{D}_{Re}(\mathbf{u}, p) \equiv 2 \int_{\Gamma_{cyl}} \left[-p\mathbf{n} + \frac{2}{Re} \mathbf{D}(\mathbf{u}) \cdot \mathbf{n} \right] \cdot \mathbf{e}_x d\ell, \quad (16)$$

$$F_y = \mathcal{L}_{Re}(\mathbf{u}, p) \equiv 2 \int_{\Gamma_{cyl}} \left[-p\mathbf{n} + \frac{2}{Re} \mathbf{D}(\mathbf{u}) \cdot \mathbf{n} \right] \cdot \mathbf{e}_y d\ell. \quad (17)$$

where Γ_{cyl} is the boundary of the cylinder. The factor 2 stands for the fact that our numerical domain is half the physical domain.

Mesh adaptation procedure Let's consider now the matlab code reported in figure 1. First we build an initial mesh (line 1), and compute base flow solutions for increasing values of the Reynolds number up to $Re = 60$ (lines 3-9). Then we perform the mesh adaptation with the structural sensitivity, as explained in a previously (line 13). The resulting mesh, depicted in figure 9, is used for the rest of the computations presented in this paper (except for displaying the eigenmode in figure 4a). Appendix D presents additional test regarding mesh convergence, and demonstrate that results obtained with the resulting mesh are trustable within 0.1% accuracy for the eigenvalue, while requiring a very reasonable number of grid points compared to previous studies of this problem.

Base flow Having thus produced a convenient mesh, we can now illustrate the properties of the base flow as function of Reynolds number. Figure 1 shows how to compute and plot with StabFem the two most commonly studied quantities, namely the recirculation length $L_x(Re)$, i.e. the location of the stagnation point at the rear of the recirculation region, and the drag coefficient $C_x(Re)$. Note that the object *bf* is defined as a structure with fields *Drag* and *Lx*. The resulting plots are given in figure 3, and are in good agreement with known results for this classical problem. In particular, for low Reynolds, the recirculation $L_x(Re)$ is equal to 0.5 (which is the radius of the cylinder) indicating the

⁴ Remark that F_x and F_y are actually nondimensional forces per unit length. For a cylinder of diameter D and length L (assuming $L \gg D$ so that the assumption of 2D flow makes sense), the corresponding dimensional forces are $F_x^* = \rho U_\infty^2 D L F_x$ and $F_y^* = \rho U_\infty^2 D L F_y$. Alternatively, one may characterize the forces through the drag and lift coefficients C_x and C_y . With the usual convention, The connection between the nondimensional forces and the force coefficients is $C_x = 2F_x$; $C_y = 2F_y$.

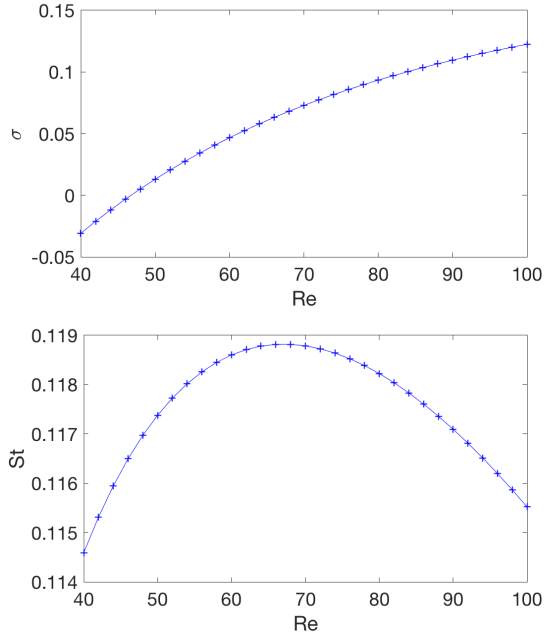


Fig. 4. Growth rate σ (a) and Strouhal number $St = \omega/2\pi$ (b) as function of Reynolds number

absence of a recirculation region. The latter appears for $Re > 4.8$, in accordance with known results.

An illustration of the structure of the base flow is given in figure 2, for the case $Re = 60$. The contour line on this plot corresponds to the iso-level $u_x = 0$, and allows to visualize the recirculation region associated to this base flow. In accordance with figure 3(b), for $Re = 60$ the recirculation length is $L_x \approx 4.07$.

Linear stability results We investigate the stability of the base flow fields by performing a parametric study of the eigenproblem (11). In this way, we determine the critical Reynolds number Re_c at which the steady base flow first becomes unstable: to this end it is useful to remember that a flow state is linearly unstable when the real part of the leading eigenvalue, i.e. the growth rate, is positive. Figure 4 shows growth rate and the Strouhal number $St = a\omega/2\pi U_\infty$ as a function of the Reynolds number. It is easy to check that the critical Reynolds number is about 47 for the first mode. The associated direct eigenmode is depicted in figure 5. The spatial structure of this mode extends downstream of the bluff body and is characterized by streamwise extended spatial disturbances. On the other hand, the adjoint mode is highly localized near the cylinder on the upper (and lower) side of the body surface. We recall that the adjoint field provides useful information about the mechanism to flow receptivity to momentum forcing and mass injection. We note also that this receptivity decays rapidly both upstream and downstream of the bluff body.

The structural sensitivity field displayed in figure 5c) is obtained by evaluating eq. 15. In particular, we plot the spectral norm of the sensitivity tensor, it gives the maximum possible coupling among the velocity components. This

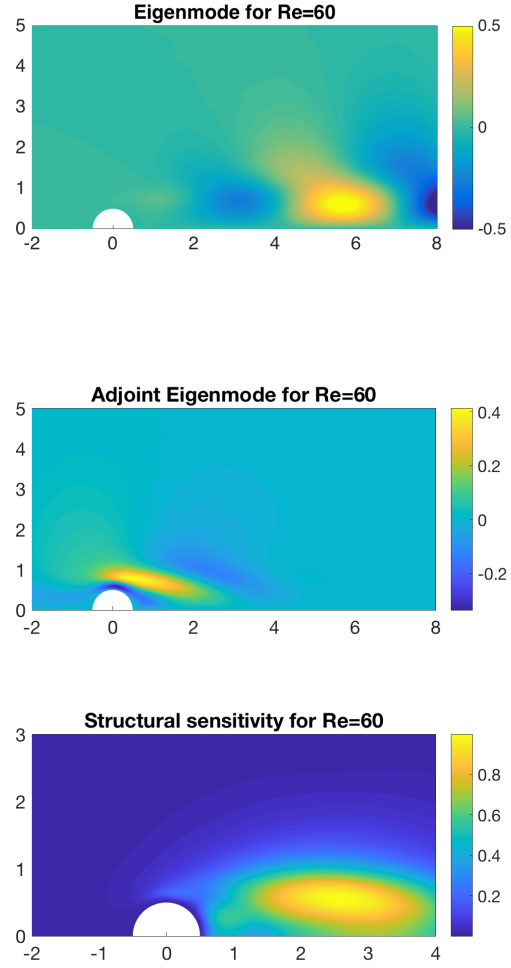


Fig. 5. Contour plot of the streamwise velocity component: (a) (Direct) Eigenmode; (b) Adjoint mode and (c) Structural sensitivity field for the cylinder's wake at $Re = Re_c = 46.7$.

spatial map can be used to identify the flow region where the instability mechanism acts.

4 Nonlinear global stability approaches

In the past decade, efforts have been devoted to extend the range of validity of global approaches into the nonlinear regime for $Re > Re_c$, with the double objective to describe the properties of the limit cycle reached after saturation and to derive amplitude equations describing the transient dynamics towards this cycle. The two main milestones in this direction are the *weakly nonlinear model* (WNL) of Sipp & Lebedev [5] and the *self-consistent model* (SC) of Mantič-Lugo et al [1]. In this review, we will address only the first of the two questions, namely the description of the saturated cycle, and leave aside the question of transient dynamics. We will successively review the two aforementioned models, in a simplified formulation devoted

to describe only the saturated cycle. We also provide a simple implementation of these two models. Finally, in line with the previous section, we will again illustrate with results obtained for the wake of a cylinder.

4.1 General definitions in the nonlinear regime

In the nonlinear regime, the *base flow* introduced in the linear theory is not directly accessible and no longer relevant, especially when the oscillation amplitudes become large. Instead, one may define a *mean flow* by time-averaging:

$$\mathbf{u}_m(\mathbf{x}) = \frac{1}{T} \int_0^T \mathbf{u}(\mathbf{x}, t) dt, \quad (18)$$

where $T = 2\pi/\omega$ is the period of the oscillation cycle. The difference between the instantaneous solution and the mean flow is then called the *nonlinear perturbation*, defined as

$$\mathbf{u}'(\mathbf{x}, t) = \mathbf{u}(\mathbf{x}, t) - \mathbf{u}_m(\mathbf{x}). \quad (19)$$

A convenient measure of the unsteady part of the flow, which has been adopted in both the WNL and SC models, is the energy-amplitude, defined as the square-root of the total energy associated to the nonlinear perturbation:

$$A_E = \sqrt{\frac{1}{T} \int_0^T \left(\int_{\Omega} |\mathbf{u}'|^2 dS \right) dt}. \quad (20)$$

In the next sections we will document the predictions of the WNL and SC models regarding the quantities A_E and L_x adopted in past studies. In addition, we will document two other quantities of practical interest : the Drag and Lift forces F_x and F_y exerted on the cylinder. Both are periodic functions of time and; owing to symmetry consideration, the drag contains only even harmonics and the lift only odd harmonics:

$$F_x = F_{x,0} + \sum_{n=1}^{\infty} (F_{x,2n,c} \cos(2n\omega t) + F_{x,2n,s} \sin(2n\omega t)), \quad (21)$$

$$F_y = \sum_{n=1}^{\infty} (F_{y,2n-1,c} \cos((2n-1)\omega t) + F_{y,(2n-1),s} \sin((2n-1)\omega t)). \quad (22)$$

In the sequel we will focus on the *mean drag* $F_{x,0}$ and on the fundamental components of the lift $F_{y,1,c}$ and $F_{y,1,s}$. These quantities are easily extractible from a numerical simulation or an experiment, and we will show how they can be predicted from the nonlinear global approaches.

In this part, to simplify the notations, we symbolically write the Navier-Stokes equations, as $\partial_t \mathbf{u} = \mathcal{N}\mathcal{S}(\mathbf{u})$, therefore dropping the systematic reference to the incompressibility constraint and associated pressure field. The same is done with the linearized operator $\mathcal{L}\mathcal{N}\mathcal{S}_{\mathbf{U}}(\mathbf{u})$.

4.2 The weakly nonlinear model

WNL model: analysis We first review the weakly nonlinear model of Sipp & Lebedev [5], also discussed by Gallaire et al. [12]. The initial derivation of [5] makes use of a multiple scale method in order to obtain an amplitude equation. This complete analysis is reproduced in appendix B. In the present paragraph, we give a simplified derivation of this model restricted to the description of the periodic saturated cycle. The starting point can be taken as the following expansion of the velocity flow field:

$$\begin{aligned} \mathbf{u} = & \mathbf{u}_{bc} + \varepsilon \left[A_{wnl} \hat{\mathbf{u}} e^{i(\omega_c + \varepsilon^2 \omega_\varepsilon)t} + c.c. \right] \\ & + \varepsilon^2 \left[\mathbf{u}_\varepsilon + |A_{wnl}|^2 \mathbf{u}_{2,0} + \left(A_{wnl}^2 \mathbf{u}_{2,2} e^{2i(\omega_c + \varepsilon^2 \omega_\varepsilon)t} + c.c. \right) \right] \\ & + O(\varepsilon^3), \end{aligned} \quad (23)$$

This expansion is built as an asymptotic expansion in terms of the small parameter $\varepsilon = \sqrt{1/Re_c - 1/Re}$ corresponding to the distance to the critical Reynolds. The zero-order term \mathbf{u}_{bc} is the base flow at the threshold Re_c .

In the first-order term, $\hat{\mathbf{u}}$ is the neutral eigenmode at Re_c conveniently normalized (see discussion in appendix B), A_{wnl} an amplitude, ω_c the frequency predicted by the linear approach at $Re = Re_c$ and ω_ε a small deviation of the frequency.

The second-order term contains three contributions: \mathbf{u}_ε is the modification to the base flow related to the increase of Re , $\mathbf{u}_{2,0}$ represents the nonlinear interaction of $\hat{\mathbf{u}}$ with its conjugate, $\mathbf{u}_{2,2}$ the nonlinear interaction of $\hat{\mathbf{u}}$ with itself. These three terms are computed as solutions of nonsingular linear systems (see eqs. 38, 39, 40 in appendix B).

At $O(\varepsilon^3)$, compatibility conditions have to be imposed to ensure that the problem is correctly posed. These conditions lead to an “amplitude equation” which relates the amplitude A_{wnl} to three parameters Λ, v_0 and v_2 which depend uniquely on \mathbf{u}_ε , $\mathbf{u}_{2,0}$ and $\mathbf{u}_{2,2}$, respectively (see equations 42, 43 and 44 in appendix B). Restricting to the description of the limit cycle, the “amplitude equation” takes the form:

$$i\omega_\varepsilon A_{wnl} = \Lambda A_{wnl} - (v_0 + v_2) |A_{wnl}|^2 A_{wnl}. \quad (24)$$

The amplitude A_{wnl} and the correction to the frequency are then determined by considering the real and imaginary parts of this equation, leading to $|A_{wnl}| = \sqrt{\frac{\Lambda_r}{v_{0,r} + v_{2,r}}}$ and $\omega_\varepsilon = \Lambda_i - \Lambda_r \frac{v_{0,i} + v_{2,i}}{v_{0,r} + v_{2,r}}$ where the subscripts r and i represent the real and imaginary parts. Reintroducing the scaling, the amplitude $|A| = \varepsilon |A_{wnl}|$ and the frequency ω of the limit cycle are thus predicted as

$$|A| = \varepsilon |A_{wnl}| = \sqrt{\frac{\Lambda_r}{v_{0,r} + v_{2,r}}} \sqrt{\frac{1}{Re_c} - \frac{1}{Re}}, \quad (25)$$

```

1 % WNL model
2 [bf,em]=SF_FindThreshold(bf,em); Omegac=imag(em.lambda);
3 [ev,em] = SF_Stability(bf,'shift',1i*Omegac,'nev',1,'type','A');
4 [wnl,meanflow,mode] = SF_WNL(bf,em,'Retest',47.,'Normalization','L');
5
6 epsilon2_WNL = 0.003:.0001:.005;
7 Re_WNL = 1./(1/Rec - epsilon2_WNL);
8 A_WNL = wnl.Aeps*real(sqrt(epsilon2_WNL));
9
10 % SC model
11 Re_SC = [Rec 47 47.5 48 49 50 55 60 65 70 75 80 85 90 95 100];
12 Aenergy_SC = [0];
13
14 for Re = Re_SC(2:end)
15     [meanflow,mode] = SF_SelfConsistentDirect(meanflow,mode,'Re',Re);
16     Aenergy_SC = [Aenergy_SC mode.AEnergy];
17 end
18
19 plot(Re_WNL,A_WNL,Re_SC,Aenergy_SC,'r+'); % figure 7d.

```

Fig. 6. Illustration of the procedure for nonlinear calculations using StabFem (extract from script *SCRIPT_CYLINDER_ALLFIGURES.m*).

$$\omega \equiv \omega^{(wnl)} = \omega_c + \left(\Lambda_i - \Lambda_r \frac{\mathbf{v}_{0,i} + \mathbf{v}_{2,i}}{\mathbf{v}_{0,r} + \mathbf{v}_{2,r}} \right) \left(\frac{1}{Re_c} - \frac{1}{Re} \right) \quad (26)$$

Finally, as specified above, we explain how the mean drag $F_{x,0}$ and fundamental components ($F_{y,1,c}, F_{y,1,s}$) of the oscillating lift can be predicted from the WNL approach. The mean drag can be obtained by $F_{x,0} = \mathcal{D}_{Re}(\mathbf{u}_m, p_m)$, where \mathcal{D} is the drag operator defined in 16 and $[\mathbf{u}_m, p_m]$ is the *mean flow* which corresponds to the time-average of expansion 23, namely: $[\mathbf{u}_m, p_m] = [\mathbf{u}_{bc}, p_{bc}] + \varepsilon^2 ([\mathbf{u}_\varepsilon, p_\varepsilon] + A_{wnl}^2 [\mathbf{u}_{2,0}, p_{2,0}])$. Developing the terms as an asymptotic expansion leads to:

$$F_{x,0}(Re) \approx F_{x,0,Re_c} + F_{x,0,\varepsilon} \left(\frac{1}{Re_c} - \frac{1}{Re} \right) \quad (27)$$

with $F_{x,0,Re_c} = \mathcal{D}_{Re_c}(\mathbf{u}_{bc}, p_{bc})$, and

$$F_{x,0,\varepsilon} = \mathcal{D}_{Re_c}(\mathbf{u}_\varepsilon, p_\varepsilon) - \mathcal{D}_1(\mathbf{u}_{bc}, 0) + |A_{wnl}|^2 \mathcal{D}_{Re_c}(\mathbf{u}_{2,0}, p_{2,0}).$$

Similarly the required components of the lift force are obtained by applying the lift operator \mathcal{L} defined in 17 to the order-one component of the expansion, leading to:

$$F_{y,1,c} - iF_{y,1,s} = 2|A_{wnl}| \mathcal{L}_{Re_c}(\hat{\mathbf{u}}, \hat{p}) \sqrt{\frac{1}{Re_c} - \frac{1}{Re}}. \quad (28)$$

WNL model : implementation and results for the cylinder Lines 1-8 of the script shown in figure 4.3, which is extracted from the script *SCRIPT_CYLINDER_ALLFIGURES.m*, illustrate the sequence of commands to perform the weakly nonlinear study for the cylinder wake. On line 2, we first determine

the instability threshold, and the corresponding base flow and eigenmode⁵. On line 3 we solve the adjoint problem required for some terms in the WNL formulation. On line 4, we then compute all the terms and coefficients of the WNL model. Lines 6-8 then processes the results in a way they can be plotted.

Figure 7 represent the predictions of the WNL approach regarding the frequency (expressed as a Strouhal number through $St = \omega/2\pi$), mean drag, amplitude of the oscillating lift, and energy-amplitude. As discussed in [5] and [12], when compared to DNS results the approach gives good prediction in the immediate vicinity of Re_c , but deviation appears very rapidly and disagreement is already large at $Re = 48$ (although, as discussed by [12] and also observed [13], a convenient definition of the ε improves the results). These aspects are justified by the perturbative nature of the WNL approach. The description of the limit cycle can be extended to larger Re with the approach presented next.

4.3 The Self-Consistent model

SC model : analysis We now briefly review the self-consistent model as introduced by Mantić-Lugo et al [1]. In its original exposition, the authors adopted a pseudo-eigenmode expansion of the flow as follows:

$$\mathbf{u} = \mathbf{u}_m + A_{sc} [\tilde{\mathbf{u}}_1 e^{\sigma_{sc} t + i\omega_{sc} t} + \overline{\tilde{\mathbf{u}}_1} e^{\sigma_{sc}^* t - i\omega_{sc}^* t}], \quad (29)$$

where \mathbf{u}_m is the *mean flow* defined by phase-averaging over the cycle, $\tilde{\mathbf{u}}_1$ is a pseudo-eigenvector which is normalized by

⁵This routine uses Newton iteration to directly compute the base flow, the eigenmode, the frequency and the critical Reynolds. The algorithm is very similar to the one presented for the HB, with an additional unknown (Re) and an additional constraint (normalization of the mode). The interested reader should reconstruct easily the whole procedure from the code provided.

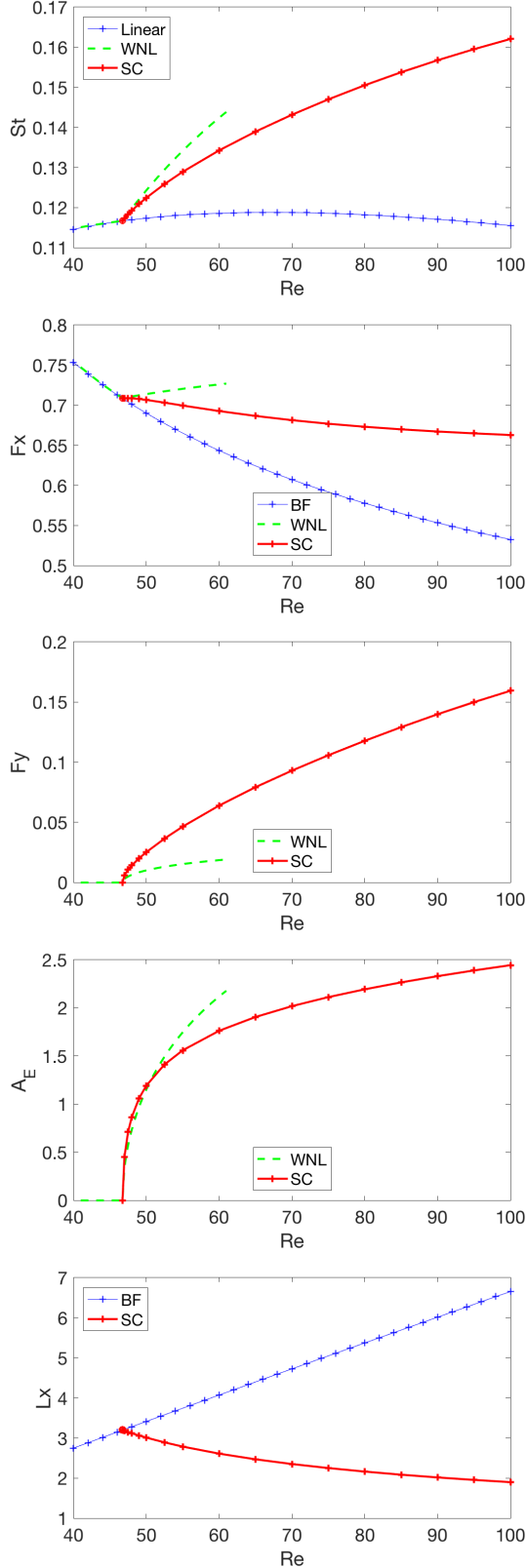


Fig. 7. Comparison between the weakly nonlinear results (WNL) the harmonic balance data (HB), and baseflow/linear results : Strouhal number (a), Mean drag (b), amplitude of oscillating lift (c), Energy-amplitude of the nonlinear perturbation (d) and recirculation length of mean/base flows (e).

the condition $\|\bar{\mathbf{u}}_1\| = 1/\sqrt{2}$, $\bar{\mathbf{u}}_1$ is its complex conjugate, A_{sc} is an amplitude parameter directly related to the energy of the oscillating flow, and $\lambda_{sc} = \sigma_{sc} + i\omega_{sc}$ is a pseudo-eigenvalue which depends upon the parameter A_{sc} .

The original version of the model (discussed with some more details in appendix C) allowed to obtain an amplitude equation relating the instantaneous growth rate σ as function of the amplitude A_{sc} . However, if we are simply interested in the properties of the limit cycle, not the transient, we may recast the self-consistent model in a simpler way.

We thus start with a truncated Fourier decomposition of the limit cycle under the form:

$$\mathbf{u} = \mathbf{u}_m + \mathbf{u}_{1,c} \cos(\omega t) + \mathbf{u}_{1,s} \sin(\omega t), \quad (30)$$

where $\mathbf{u}_{1,c}$ and $\mathbf{u}_{1,s}$ are two *real* fields describing the cycle at two instants separated by a quarter-period of oscillation, and ω is the (real) oscillation frequency of the limit cycle (which is not known a priori). The connection with the definition of Mantič-Lugo is as follows:

$$(\mathbf{u}_{1,c} - i\mathbf{u}_{1,s}) = 2A_{sc}\bar{\mathbf{u}}_1. \quad (31)$$

Injecting this ansatz into the Navier-Stokes equations and taking the mean value and the first Fourier component leads to the following coupled equations:

$$\mathcal{N}(\mathbf{u}_m) = \frac{\mathcal{C}(\mathbf{u}_{1,c}, \mathbf{u}_{1,c}) + \mathcal{C}(\mathbf{u}_{1,s}, \mathbf{u}_{1,s})}{4}, \quad (32a)$$

$$\omega \mathbf{u}_{1,s} = \mathcal{L} \mathcal{N}_{\mathbf{u}_m}(\mathbf{u}_{1,c}), \quad (32b)$$

$$-\omega \mathbf{u}_{1,c} = \mathcal{L} \mathcal{N}_{\mathbf{u}_m}(\mathbf{u}_{1,s}). \quad (32c)$$

To allow resolution we need an extra equation to fix the *phase* of the cycle. Several choices are possible, but a convenient one is to decide that the instant $t = 0$ corresponds to a maximum of the lift force. This condition reads:

$$\mathcal{L}_{Re}(\mathbf{u}_{1,s}) = 0. \quad (33)$$

Note that the amplitude A_{sc} , which was considered as a key parameter in the original model of [1], does not appear in the simplified version discussed here. This parameter can easily be computed a posteriori as $A_{sc} = \sqrt{2 \int_{\Omega} (|\mathbf{u}_{1,c}|^2 + |\mathbf{u}_{1,s}|^2) dS}$.

SC model: implementation and results for a cylinder

Mathematically, the system (32a, 32b, 32c, 33) for the unknown $[\mathbf{u}_m, \mathbf{u}_{1,c}, \mathbf{u}_{1,s}, \omega]$ is well posed. Instead of the double-loop resolution procedure of [1], we propose a direct resolution using a Newton iteration just as explained for the base flow in section 2. We then assume that we know a “guess”:

$$[\mathbf{u}_m, \mathbf{u}_{1,c}, \mathbf{u}_{1,s}, \omega] = [\mathbf{u}_m^g, \mathbf{u}_{1,c}^g, \mathbf{u}_{1,s}^g, \omega^g] + [\delta \mathbf{u}_m, \delta \mathbf{u}_{1,c}, \delta \mathbf{u}_{1,s}, \delta \omega].$$

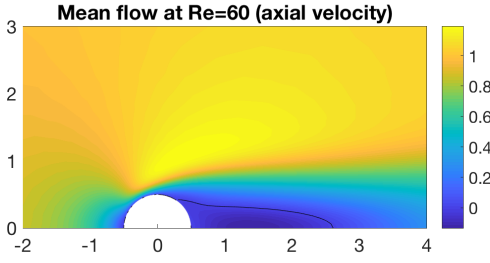


Fig. 8. Self-consistent approach for the wake of a circular cylinder: description of the MEAN FLOW for $Re = 100$.

Injecting and developing up to linear order leads to the following equations:

$$\mathcal{N}\mathcal{S}(\mathbf{u}_m^g) - \frac{1}{4}[C(\mathbf{u}_{1,c}^g, \mathbf{u}_{1,c}^g) + C(\mathbf{u}_{1,s}^g, \mathbf{u}_{1,s}^g)] + \mathcal{L}\mathcal{N}\mathcal{S}_{\mathbf{u}_m^g}(\delta\mathbf{u}_m) - \frac{1}{2}[C(\mathbf{u}_{1,c}^g, \delta\mathbf{u}_{1,c}) + C(\mathbf{u}_{1,s}^g, \delta\mathbf{u}_{1,s})] = 0, \quad (34a)$$

$$\mathcal{L}\mathcal{N}\mathcal{S}_{\mathbf{u}_m^g}(\mathbf{u}_{1,c}^g) - \omega^g \mathbf{u}_{1,s}^g - C(\delta\mathbf{u}_m, \mathbf{u}_{1,c}^g) + \mathcal{L}\mathcal{N}\mathcal{S}_{\mathbf{u}_m^g}(\delta\mathbf{u}_{1,c}) - \omega^g \delta\mathbf{u}_{1,s} - \delta\omega \mathbf{u}_{1,s}^g = 0, \quad (34b)$$

$$\mathcal{L}\mathcal{N}\mathcal{S}_{\mathbf{u}_m^g}(\mathbf{u}_{1,s}^g) + \omega^g \mathbf{u}_{1,c}^g - C(\delta\mathbf{u}_m, \mathbf{u}_{1,s}^g) + \mathcal{L}\mathcal{N}\mathcal{S}_{\mathbf{u}_m^g}(\delta\mathbf{u}_{1,s}) + \omega^g \delta\mathbf{u}_{1,c} + \delta\omega \mathbf{u}_{1,c}^g = 0, \quad (34c)$$

$$F_y(\mathbf{u}_{1,s}^g) + F_y(\delta\mathbf{u}_{1,s}) = 0. \quad (34d)$$

After discretization, this leads to a linear problem of the form $AX = Y$ where X is the discretized version of the unknowns $[\delta\mathbf{u}_m, \delta\mathbf{u}_{1,c}, \delta\mathbf{u}_{1,s}, \delta\omega]$, and A is a matrix of dimension $3N_{dof} + 1$, where N_{dof} is the dimension of the Taylor-Hood basis of finite elements describing each of the three $[\mathbf{u}, p]$ fields. This system is solved iteratively in the same way as explained in section 2.1 for determination of the base flow. Using the adapted mesh described in figure 2, the dimension of the system is $3N_{dof} + 1 \approx 58000$ and the resolution remains possible at very reasonable computational costs.

Lines 10-17 of the script shown in figure explain how to solve SC model using the StabFem software, for the wake of a cylinder in the range $Re \in [47 - 100]$. Note that a “guess” for the mean flow and the self-consistent mode for $Re = 47$, i.e. just above the threshold, has already been generated from the weakly nonlinear model at line 4 of the same script. This guess is used for the first step of the loop over Reynolds in lines 14-17. For next steps of the loop, continuation is done using the previous calculation as a guess.

Figure 8 illustrates the structure of the mean flow for $Re = 60$. As already identified by [1], the recirculation region associated with this mean flow is notably shorter than the one associated with the base flow (figure 2).

Figure 7 shows the comparison between the WNL (green) and SC (red) models for the quantities of interest identified in this paper, namely the Strouhal number, the

mean drag, the maximum lift, the energy-amplitude, and the recirculation length associated to the mean flow. When relevant, results concerning the base flow and the linear approach are also displayed (blue)⁶. Concerning the quantities St , A_E and L_x , differences between SC, WNL models have already been commented in [1] and [12]. The predictions of the SC models were also compared to numerical simulations results showing excellent agreement in the range $Re \in [Re_c, 100]$. Regarding the forces exerted on the body, we can remark that the predictions of the WNL and SC models rapidly depart from each other as soon as $Re - Re_c \gtrsim 1$. Comparison of these results with DNS simulations is not provided here (consistently with the objectives of the present paper) but the reader may verify that the SC model correctly predicts these quantities in the range of Reynolds number considered here.

5 Conclusion

The objective of this paper was twofold. First, we aimed at giving an up-to-date and comprehensive review on global stability approaches, both linear and nonlinear, including the most recent developments of the field. Secondly, we intended to provide an easy to use software performing all these computations from a single program. In accordance with this objective, all the figures presented in the paper can be produced by launching a single Matlab program available on the website of the project.

Although the focus here was on the reference case of 2D, incompressible flow around a cylinder, the *StabFem* software is designed to be easily customisable to a variety of other situations. The project is currently in constant development, and incorporates a growing number of other configurations. In the present status, the project incorporates test-cases for the following classes of problems:

- Incompressible flows around 2D objects, either fixed or in movement such as the case of a spring-mounted cylinder [?],
- Incompressible flows in axisymmetric geometries such as the wake of spheres and disks [?] and the flow through apertures [?],
- Compressible flow around 2D objects [?],
- Oscillations of hanging drops and liquid bridges [?]

The project is intended as collaborative, so anyone who wants to contribute is welcome !

A Details of the weak formulation

In the presentation of the numerical methods in sections 2.1 and 2.2, and introduction of the *weak form*, we have omitted an important point, namely the issue of boundary conditions. In this appendix we explain more rigorously how the weak formulation is obtained. We consider here the

⁶Figure 7 is obtained by line 19 of the script displayed in figure 4.3. The other figures are processed in a similar way. The entire set of commands to obtain all figures is provided in the script *SCRIPT_CYLINDER_ALLFIGURES.m*.

full time-dependent nonlinear Navier-Stokes equations, but the treatment of the base-flow equations and the linearised equations is essentially the same.

Noting Γ the boundary of the numerical domain, the latter can be decomposed in five parts : $\Gamma = \Gamma_{in} \cup \Gamma_{cyl} \cup \Gamma_{axis} \cup \Gamma_{out} \cup \Gamma_{lat}$. Noting $\boldsymbol{\sigma} = 2Re^{-1}\mathbf{D}(\mathbf{u}) - p\mathbf{1}$ the stress tensor, the relevant boundary conditions are as follows:

- On Γ_{in} (inlet): $\mathbf{u} = \mathbf{e}_x$ (Dirichlet).
- On Γ_{cyl} (surface of the cylinder): $\mathbf{u} = \mathbf{0}$ (Dirichlet).
- On Γ_{out} (outlet): $\boldsymbol{\sigma} \cdot \mathbf{n} = \mathbf{0}$ (Neumann).
- On Γ_{axis} (symmetry plane): $u_y = 0$ and $\sigma_{xy} = 0$ (Mixed).
- On Γ_{lat} (lateral boundary): $u_y = 0$ and $\sigma_{xy} = 0$ (Mixed).

We will introduce the following notation for integrals along any portion of the boundary Γ_i of the product of two quantities ϕ_1, ϕ_2 (either scalar or vectorial) :

$$\langle \phi_1, \phi_2 \rangle_{\Gamma_i} = \int_{\Gamma_i} \bar{\phi}_1 \cdot \phi_2 \, d\ell,$$

Instead of the simplified version 3, the more precise form of the weak formulation can be first written as follows:

$$\begin{aligned} \forall [\mathbf{v}, q], \quad \partial_t \langle \mathbf{v}, \mathbf{u} \rangle &= \langle \mathbf{v}, \mathcal{N}(\mathbf{u}, p) \rangle + \langle q, \nabla \cdot \mathbf{u} \rangle \\ &+ \frac{1}{\varepsilon} \left(\langle \mathbf{v}, \mathbf{u} \rangle_{\Gamma_{cyl}} + \langle \mathbf{v}, (\mathbf{u} - \mathbf{e}_x) \rangle_{\Gamma_{in}} + \langle v_y, u_y \rangle_{\Gamma_{axis} \cup \Gamma_{lat}} \right) \\ &+ \langle \mathbf{v}, \boldsymbol{\sigma} \cdot \mathbf{n} \rangle_{\Gamma_{out} \cup \Gamma_{lat} \cup \Gamma_{axis}} \end{aligned} \quad (35)$$

where $\varepsilon = 10^{-30}$ is a small parameter used to impose the Dirichlet boundary conditions by penalization. An integration by parts of the pressure gradient and viscous stress terms of the Navier-Stokes equation eventually leads to the weak form effectively used in the programs *Newton2D.edp* and *Stab2D.edp*:

$$\begin{aligned} \forall [\mathbf{v}, q], \quad \partial_t \langle \mathbf{v}, \mathbf{u} \rangle &= -\langle \mathbf{v}, C(\mathbf{u}, \mathbf{u})/2 \rangle - 2Re^{-1} \langle \mathbf{D}(\mathbf{v}) : \mathbf{D}(\mathbf{u}) \rangle \\ &+ \langle \nabla \cdot \mathbf{v}, p \rangle + \langle q, \nabla \cdot \mathbf{u} \rangle \\ &+ \frac{1}{\varepsilon} \left(\langle \mathbf{v}, \mathbf{u} \rangle_{\Gamma_{cyl}} + \langle \mathbf{v}, (\mathbf{u} - \mathbf{e}_x) \rangle_{\Gamma_{in}} + \langle v_y, u_y \rangle_{\Gamma_{axis} \cup \Gamma_{lat}} \right) \end{aligned} \quad (36)$$

Note that the Neumann boundary conditions do not appear any more thanks to the integration by parts.

B Additional details of the weakly nonlinear approach

B.1 Derivation of the amplitude equation using multiple-scale approach

The initial derivation of [5] makes use of a multiple scale method in order to obtained an amplitude equation. The starting point can be taken as the following expansion of the velocity flow field:

$$\begin{aligned} \mathbf{u} &= \mathbf{u}_{bc} + \varepsilon [A_{wnl}(\tau) \hat{\mathbf{u}} e^{i\omega_c t} + c.c.] \\ &+ \varepsilon^2 [\mathbf{u}_\varepsilon + |A_{wnl}(\tau)|^2 \mathbf{u}_{2,0} + (A_{wnl}(\tau)^2 \mathbf{u}_{2,2} e^{2i\omega_c t} + c.c.)] \\ &+ O(\varepsilon^3), \end{aligned} \quad (37)$$

Note that compared to the simplified version given in the main text by eq. 23, the amplitude A_{wnl} depends upon a slow time scale $\tau = \varepsilon^2 t$.

Substituting the expansion 37 into the Navier-Stokes equations 1 and grouping terms multiplied by the same power of ε , a hierarchy of equations is obtained. The order ε^0 gives directly the base flow at Re_c . The order ε^1 corresponds to the linear neutral eigenmode as computed in the first part of this article. The order ε^2 contains three terms respectively computed as the solutions of the following linear problems:

$$\mathcal{L} \mathcal{N}_{\mathbf{u}_{bc}}(\mathbf{u}_\varepsilon) - 2\nabla \cdot \mathbf{D}(\mathbf{u}_{bc}) = 0, \quad (38)$$

$$\mathcal{L} \mathcal{N}_{\mathbf{u}_{bc}}(\mathbf{u}_{2,0}) = C(\hat{\mathbf{u}}, \bar{\hat{\mathbf{u}}}), \quad (39)$$

$$\mathcal{L} \mathcal{N}_{\mathbf{u}_{bc}}(\mathbf{u}_{2,2}) - 2i\omega_c \mathbf{u}_{2,2} = \frac{1}{2} C(\hat{\mathbf{u}}, \hat{\mathbf{u}}). \quad (40)$$

Finally, compatibility conditions, given by the Fredholm's alternative, are imposed at order ε^3 to remove the secular terms, leading to an amplitude equation, known as Stuart-Landau equation:

$$\frac{\partial A_{wnl}}{\partial \tau} = \Lambda A_{wnl} - (v_0 + v_2) |A_{wnl}|^2 A_{wnl}, \quad (41)$$

where coefficients Λ , v_0 and v_2 are given by

$$\Lambda = -\frac{\langle \hat{\mathbf{u}}^\dagger, (C(\mathbf{u}_\varepsilon, \hat{\mathbf{u}}) + 2\nabla \cdot \mathbf{D}(\hat{\mathbf{u}})) \rangle}{\langle \hat{\mathbf{u}}^\dagger, \hat{\mathbf{u}} \rangle}, \quad (42)$$

$$v_0 = \frac{\langle \hat{\mathbf{u}}^\dagger, C(\mathbf{u}_{20}, \hat{\mathbf{u}}) \rangle}{\langle \hat{\mathbf{u}}^\dagger, \hat{\mathbf{u}} \rangle}, \quad (43)$$

$$v_2 = \frac{\langle \hat{\mathbf{u}}^\dagger, C(\mathbf{u}_{22}, \bar{\hat{\mathbf{u}}}) \rangle}{\langle \hat{\mathbf{u}}^\dagger, \hat{\mathbf{u}} \rangle}, \quad (44)$$

B.2 Normalisation of the eigenmode

A key issue in the weakly nonlinear expansion is that the definition of the amplitude depends upon a normalization choice of the eigenmodes. Several choices are possible. In the literature three possibilities have been used:

First, [5] normalized the eigenmode by assuming a specified value to the y-component of the velocity at one point, namely:

$$\hat{u}_y(1, 0) = 0.4612. \quad (45)$$

The advantage of this choice is that the amplitude $|A|$ is then an approximate measure of the energy of the perturbation: $|A| \approx A_E$.

Secondly, [12] proposed the following normalization choice:

$$\int_{\Omega} |\hat{\mathbf{u}}|^2 d\mathbf{x} = \frac{1}{2}. \quad (46)$$

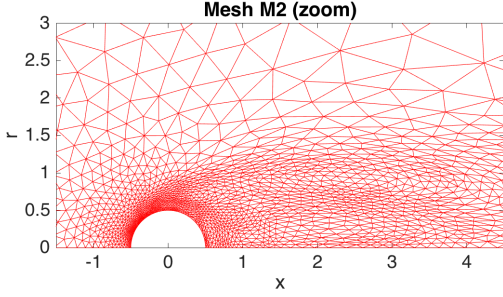
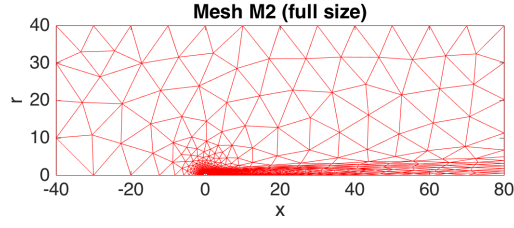


Fig. 9. Illustration of the structure of mesh \mathbf{M}_2 (adapted to both the base flow and structural sensitivity).

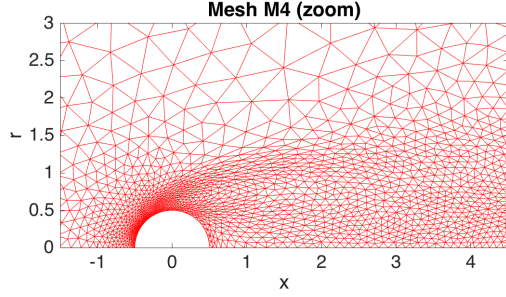
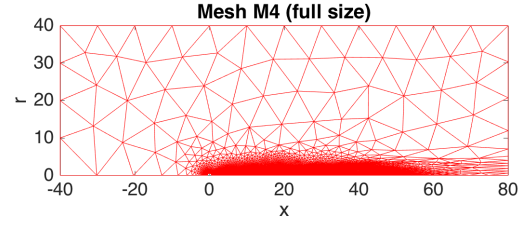


Fig. 10. Illustration of the structure of mesh \mathbf{M}_4 (adapted to both the base flow and direct eigenmode).

This directly leads to $|A| = A_E$, so this normalisation seems equivalent to the previous one.

Thirdly, following [?], another convenient choice is to normalize the eigenmode with its lift force:

$$\mathcal{D}_{Re_c}(\hat{\mathbf{u}}, \hat{p}) = \frac{1}{2}. \quad (47)$$

The advantage of this choice is that the amplitude $|A|$ is then an direct measure of the fundamental lift. In effect, eq. 28 directly leads to $F_{y,1,c} = |A|$, $F_{y,1,s} = 0$.

In our implementation of the WNL approach, we allowed to choose the normalization convention, as seen in line 3 of figure 4.3. In table 1 we give the predictions of the WNL approach using the three normalization choices. We can note that the coefficients v_0 and v_2 strongly depend on the normalization choice. On the other hand, the frequency deviation ω_e and the λ coefficient, and the term $F_{x,0,e}$ related to the dependency of mean drag with deviation from the threshold are independent upon the normalization.

Considering the lift force, columns 7 and 8 of the table show that the different choices of normalization give different values for the coefficients $F_{1,y,c}$ and $F_{1,y,s}$. However, the sin-cos expansion of the lift force can be recast as $F_y = (F_{y,1,c} \cos \omega t + F_{y,1,s} \sin \omega t) = |F_{y,1}| \cos(\omega t + \varphi)$ with $|F_{y,1}| = \sqrt{F_{y,1,c}^2 + F_{y,1,s}^2}$. The last column of the table confirms that the three possible normalization choices effectively lead to the same values of $|F_{y,1}|$.

C Additional details about the self-consistent method

NOT SURE IF THIS PART SHOULD BE KEPT OR NOT...

The original form of the SC model given by [?] was obtained by introducing the decomposition (29) into the Navier-Stokes equations, leading to :

$$\mathcal{N}(\mathbf{u}_m) - A^2 \mathcal{C}(\tilde{\mathbf{u}}_1, \overline{\tilde{\mathbf{u}}_1}) = 0, \quad (48a)$$

$$(\sigma_{sc} + i\omega_{sc})\tilde{\mathbf{u}}_1 = \mathcal{L}\mathcal{N}_{\mathbf{u}_m}(\tilde{\mathbf{u}}_1). \quad (48b)$$

Equation (48a) provides the mean flow field \mathbf{u}_m while the pseudo-eigenpairs $(\lambda_{sc}, \tilde{\mathbf{u}}_1)$ can be computed by solving the eigenvalue problem (48b). [?] Initially proposed a resolution method involving two imbricated loops, which is advantageously replaced by the direct Newton resolution of section 4.3.

The self-consistent model has the following properties:

- For $\ll 1$ it is equivalent to the linear eigenvalue problem (9), and the generalized eigenvalue coincides with the one predicted by linear stability : $\sigma_{sc} + i\omega_{sc} = \sigma_{lin} + i\omega_{lin}$.
- For $\sigma_{sc} = 0$ (corresponding to a specific choice of the amplitude $A = A_c$), the expansion (29) is equivalent to the Fourier expansion ?? taken as the starting point in the present paper.
- For $0 < A < A^c$, the resolution leads to a relation $\sigma_{sc}(A); \omega_{sc}(A)$ such that $0 < \sigma_{sc}(A) < \sigma_{lin}$. Although in this case the expansion (29) cannot represent the flow for all t , Mantič-Lugo et al [1] argued that the relation

Norm.	λ	v_0	v_2	ω_ϵ	$F_{x,0,\epsilon}$	$F_{y,1,c}/\epsilon$	$F_{y,1,s}/\epsilon$	$ F_{y,1} /\epsilon$
[5]	$9.10988 + 3.28004i$	$9.3996 - 32.0289i$	$-0.305116 - 0.866118i$	36.2307	5.2848	0.0349973	-0.536113	0.537254
[12]	$9.10988 + 3.28004i$	$(0.488701 - 1.66524i) \times 10^{-3}$	$(-1.58635 - 4.50309i) \times 10^{-5}$	36.2307	5.2848	0.537254	0	0.537254
[?]	$9.10988 + 3.28004i$	$32.62 - 111.152i$	$-1.05886 - 3.00574i$	36.2307	5.2848	0.537254	0	0.537254

Table 1. Results of the WNL approach for three different choices of eigenmode normalization.

between σ_{SC} and A can be used to build an amplitude equation which captures the transient approach to the limit cycle.

D Mesh convergence : efficiency of mesh adaptation and effect of domain size

This appendix presents complementary results obtained using various mesh designs. All the results can be obtained using the following program available on the StabFem website : *SCRIPT_CYLINDER_MESHCONVERGENCE.m*.

D.1 Efficiency of the mesh adaptation process

As discussed in section 3, the mesh adaptation proves to be an extremely efficient way to obtain significant results with very reasonable meshes. The objective of this paragraph is to demonstrate this point by comparing the efficiency of several ways to perform mesh adaptation.

For this purpose, 5 meshes were generated. Mesh \mathbf{M}_1 was adapted on the *base flow* obtained for $Re = 60$. Mesh \mathbf{M}_2 was adapted to both the base flow and structural sensitivity. Mesh \mathbf{M}_3 was obtained by a subsequent refinement of mesh \mathbf{M}_2 , splitting all triangles in four subtriangles, therefore doubling the effective density of the mesh. Meshes \mathbf{M}_4 and \mathbf{M}_5 were obtained by adapting to the structure of the direct eigenmode and of the adjoint eigenmode. In each case, the adaptmesh process was repeated twice in order to ensure a correct convergence.

Figures 9 and 10 illustrate the structure of meshes \mathbf{M}_2 and \mathbf{M}_4 . As can be observed, these two mesh adaptation strategies lead to meshes with comparable densities in the region close to the cylinder. On the other hand, when moving downwards in the wake, mesh \mathbf{M}_2 quickly gets rather coarse, while mesh \mathbf{M}_4 maintains a significant density

Table 2 gives additional details about the geometry of these meshes. In particular, we document the minimum and maximum cell size, as well as the cell size at four point A,B,C,D defined with by their coordinates as follows : $(x_A, y_A) = (0, 0.5)$ (within the boundary layer at the cylinder wall); $(x_B, y_B) = (2.5, 0.5)$ (in the region of maximum structural sensitivity); $(x_C, y_C) = (4, 0)$ (in the near wake); $(x_D, y_D) = (10, 0)$ (in the far wake). Results confirm that mesh all meshes have similar densities in the near wake (cell size at points A,B,C are comparable) while \mathbf{M}_4 has maximum resolution in the far wake (in the vicinity of point D).

Table 3 compares the results obtained with the five meshes. For base-flow characteristics L_x and F_x , all values agree with a relative dispersion of less than 0.15%, confirming that all adaptation strategies are successful to correctly compute the base flow. The performances of meshes for linear stability calculations can then be evaluated by comparing the eigenvalues. Meshes \mathbf{M}_2 to \mathbf{M}_5 all give values within less than 0.1% dispersion. The value obtained with mesh \mathbf{M}_1 , which is not adapted to the eigenmode, is a bit farther from the others but still rather good. The table also displays results allowing to compare the performances of meshes for nonlinear self-consistent calculations. As for the frequency and the maximum lift, meshes \mathbf{M}_2 to \mathbf{M}_5 again give almost identical values within less than 0.1% dispersion. The dispersion is much larger concerning the energy-amplitude of the perturbation A_E displayed in the last column. Only the mesh \mathbf{M}_4 is able to correctly compute this quantities, while all other meshes significantly underestimate it. This is not surprising since this quantity is an integral one which depends upon the structure of the nonlinear perturbation in the whole wake, not only the near-wake region.

From this study we can conclude that if we are only interested in predicting the frequency of the mode and the forces exerted on the cylinder (in both linear and nonlinear regimes), the strategy of mesh adaptation to both base flow and structural sensitivity (mesh \mathbf{M}_2) is the most efficient and leads to a very light mesh (here only 2048 points). On the other hand, if we are interested in describing the structure of the perturbation in the whole domain (and being able to correctly evaluate its energy), mesh adaptation to the eigenmode structure is preferable. However this second strategy produces a much heavier mesh (here 12080 point).

D.2 Effect of domain size and boundary conditions

As already identified in several previous studies, the size of the domain and the type of boundary conditions applied at the boundaries have a notable impact on the results. To illustrate this, we designed three additional meshes. All were obtained through adaptation to base flow and sensitivity, just as mesh \mathbf{M}_2 . Meshes \mathbf{M}_6 and \mathbf{M}_7 are respectively twice smaller and twice larger than the reference one. \mathbf{M}_8 has the same dimension as the reference case but the boundary condition at the lateral boundary Γ_{lat} is replaced by a less restrictive slip condition.

Even though the domain size of the reference case

Mesh	N_p	N_{dof}	δ_{min}	δ_{max}	δ_A	δ_B	δ_C	δ_D
M₁ (Adapt on base flow)	1429	12545	0.0131	14.33	0.0259	0.514	0.819	1.067
M₂ (Adapt on sensitivity)	2038		0.0155	14.17	0.02826	0.2046	0.3909	1.2014
M₃ (Adapt on sensitivity, split)	7974		0.0077	7.1	0.014	0.1	0.2	0.6
M₄ (Adapt on mode)	12080		0.00825	124.61	0.0229	0.143	0.0993	0.0934
M₅ (Adapt on adjoint)	3813	33715	0.0081	14.4	0.0123	0.156	0.166	1.44

Table 2. Description of meshes used for validation of mesh adaptation strategy : number of vertices N_p ; number of degrees of freedom of the P2-P2-P1 Taylor-hood basis N_{dof} ; cell size (minimum and value, and value at four characteristic point A,B,C,D as defined in the text).

Mesh	L_x	F_x	λ	$L_{x,SC}$	$F_{x,SC}$	ω_{SC}	$F_{y,1,c}$	A_E
M₁	4.0733	0.6431	$0.047056 + 0.74416i$	2.6073	0.69277	0.84334	0.1298	1.8301
M₂	4.075	0.64348	$0.046719 + 0.74489i$	2.	0.69246	0.84351	0.12789	1.7134
M₃	4.0772	0.64391	$0.04684. + 0.74511i$	2.6141	0.69338	0.84383	0.12799	2.048
M₄	4.0748	0.64402	$0.04676 + 0.74502i$	2.613	0.690338	0.84371	0.12809	2.5905
M₅	4.0772	0.64384	$0.04665 + 0.74530i$	2.6146	0.6932	0.84333	0.1276	2.5971

Table 3. Results for mesh adaptation strategy ($Re = 60$) : Base-flow characteristics L_x and F_x , linear eigenvalue λ , Nonlinear self-consistent model characteristics ω_{SC} , $F_{y,1,c}$ and A_E . All the results can be obtained using the matlab program *SCRIPT_CYLINDER_MESHCONVERGENCE.m*.

Mesh	N	L_x	F_x	λ	$L_{x,SC}$	$F_{x,SC}$	ω_{SC}	$F_{Y,SC}$	$A_{E,SC}$
M₂ (ref)	7974	4.0772	0.64391	$0.04684. + 0.74511i$	2.6141	0.69338	0.84383	0.12799	2.048
M₆ $[-20, 40]_x[0, 20]$	7437	4.108	0.64987	$0.048368. + 0.74952i$	2	0.69957	0.85015	0.13125	2.3638
M₇ $[-80, 160]_x[0, 80]$	7480	4.0641	0.64129	$0.046271 + 0.74341i$	2	0.69069	0.84159	0.12653	2.4453
M₈ (slip conditions)	7056	4.0467	0.66295	$0.049216 + 0.76553i$	2	0.69241	0.8438	0.12716	2.3202

Table 4. Comparison of the performances of several meshes with variable dimensions and different boundary conditions

(namely $[-40, 80] \times [0, 40]$) may appear large, the table shows that confinement effects are still present. The quantity which appears the most sensible to domain size and/or boundary conditions is the imaginary part of the linear eigenvalue. Interestingly, the nonlinear SC results appears to be more robust with respect to confinement effects than linear ones. In effect, values for nonlinear frequency ω_{SC} and the maximum lift $F_{y,1,c}$ obtained with meshes **M₂**, **M₇** and **M₈** agree with less than 0.3% dispersion.

References

- [1] Mantič-Lugo, V., Arratia, C., and Gallaire, F., 2014. “Self-consistent mean flow description of the nonlinear saturation of the vortex shedding in the cylinder wake”. *Phys. Rev. Lett.*, **113**, p. 084501.
- [2] Drazin, P., and Reid, W., 2004. *Hydrodynamic Stability*. Cambridge University Press.
- [3] Giannetti, F., and Luchini, P., 2007. “Structural sensitivity of the first instability of the cylinder wake”. *J. Fluid Mech.*, **581**, pp. 167–197.
- [4] Marquet, O., Sipp, D., and Jacquin, L., 2008. “Sensitivity analysis and passive control of cylinder

- flow”. *J. Fluid Mech.*, **615**, pp. 221–252.
- [5] Sipp, D., and Lebedev, A., 2007. “Global stability of base and mean-flows: a general approach and its applications to cylinder and open cavity flows”. *J. Fluid Mech.*, **593**, pp. 333–358.
 - [6] Luchini, P., and Bottaro, A., 2014. “Adjoint equations in stability analysis”. *Annu. Rev. Fluid Mech.*, **46**, pp. 493–517.
 - [7] Schmid, P. J., and Henningson, D. S., 2001. *Stability and Transition in Shear Flows*. Springer-Verlag, New York.
 - [8] Chomaz, J.-M., 2005. “Global instabilities in spatially developing flows: Non-normality and nonlinearity”. *Annu. Rev. Fluid Mech.*, **37**, pp. 357–392.
 - [9] Schmid, P. J., 2007. “Nonmodal stability theory”. *Annu. Rev. Fluid Mech.*, **39**, pp. 129–162.
 - [10] Arnoldi, W. E., 1951. “The principle of minimized iterations in the solution of the matrix eigenvalue problem”. *Quart. Appl. Math.*, **9**, pp. 17–29.
 - [11] Hecht, F., 1998. “The mesh adapting software: bamg”. *INRIA report*.
 - [12] Gallaire, F., Boujo, E., Mantič-Lugo, V., Arratia, C., Thiria, B., and Meliga, P., 2016. “Pushing amplitude equations far from threshold: application to the supercritical hopf bifurcation in the cylinder wake”. *Fluid. Dyn. Res.*, **48**, p. 061401.
 - [13] Tchöufag, J., Fabre, D., and Magnaudet, J., 2015. “Weakly nonlinear model with exact coefficients for the fluttering and spiraling motion of buoyancy-driven bodies”. *Phys. Rev. Lett.*, **115**, p. 114501.